



How ice shelf morphology controls basal melting

Christopher M. Little,¹ Anand Gnanadesikan,² and Michael Oppenheimer^{1,3}

Received 12 November 2008; revised 21 July 2009; accepted 14 August 2009; published 5 December 2009.

[1] The response of ice shelf basal melting to climate is a function of ocean temperature, circulation, and mixing in the open ocean and the coupling of this external forcing to the sub-ice shelf circulation. Because slope strongly influences the properties of buoyancy-driven flow near the ice shelf base, ice shelf morphology plays a critical role in linking external, subsurface heat sources to the ice. In this paper, the slope-driven dynamic control of local and area-integrated melting rates is examined under a wide range of ocean temperatures and ice shelf shapes, with an emphasis on smaller, steeper ice shelves. A 3-D numerical ocean model is used to simulate the circulation underneath five idealized ice shelves, forced with subsurface ocean temperatures ranging from -2.0°C to 1.5°C . In the sub-ice shelf mixed layer, three spatially distinct dynamic regimes are present. Entrainment of heat occurs predominately under deeper sections of the ice shelf; local and area-integrated melting rates are most sensitive to changes in slope in this “initiation” region. Some entrained heat is advected upslope and used to melt ice in the “maintenance” region; however, flow convergence in the “outflow” region limits heat loss in flatter portions of the ice shelf. Heat flux to the ice exhibits (1) a spatially nonuniform, superlinear dependence on slope and (2) a shape- and temperature-dependent, internally controlled efficiency. Because the efficiency of heat flux through the mixed layer decreases with increasing ocean temperature, numerical simulations diverge from a simple quadratic scaling law.

Citation: Little, C. M., A. Gnanadesikan, and M. Oppenheimer (2009), How ice shelf morphology controls basal melting, *J. Geophys. Res.*, 114, C12007, doi:10.1029/2008JC005197.

1. Introduction

[2] Basal melting of Antarctic ice shelves influences ice sheet dynamics [Dupont and Alley, 2005, 2006; Payne *et al.*, 2004; Schoof, 2007]; the meltwater produced freshens and cools the circumpolar ocean [Hohmann *et al.*, 2002; Jacobs *et al.*, 1996; Orsi *et al.*, 1999]. Ocean-driven changes in melting rates or locations thus influence water mass properties, climate, and sea level. Yet the linkage between ocean heat fluxes, basal melting, and ice discharge is blurred by physical uncertainties, observational limitations, and finite computing resources [Little *et al.*, 2007]. The lack of clarity is particularly tangible in the Amundsen Sea sector of Antarctica, where increases in basal melting have triggered rapid ice shelf thinning [Shepherd *et al.*, 2004] and grounded ice loss [Payne *et al.*, 2004; Rignot, 2008]. Although upwelling near the continental shelf break may have initiated this process [Thoma *et al.*, 2008], the mechanisms linking on-shelf heat fluxes to basal melting have not been conclusively demonstrated.

[3] The complex, coupled nature of ice sheet–ocean interaction has inspired a search for key parameters governing the melting rate, ideally in a formulation suitable for a large-scale parameterization [Beckmann and Goosse, 2003; Pollard and DeConto, 2009]. Observations, simplified equation sets, and numerical models have been used to formulate scaling laws in which sub-ice shelf ocean temperature is related to area-averaged melt rates [Holland *et al.*, 2008, hereafter HJH08; MacAyeal, 1984; Rignot and Jacobs, 2002]. Despite growing support for a superlinear temperature dependence, these studies exhibit divergence (HJH08, their Figure 1), implying that some physical processes are missing. It remains unclear whether prior results are valid across different ice shelves and a large range of temperatures. Observationally derived scaling laws [Rignot and Jacobs, 2002] aggregate ice shelves with widely varying morphologies; temperature and shape dependence may be conflated. Even if an ocean temperature-based scaling is robust across ice shelves, area-integrated melt rates overlook the spatial variability of melting (as well as any glaciological response). Recent modeling and theoretical studies indicate that the distribution, rather than the total amount, of basal melting is critical to ice flow [Schoof, 2007; Walker *et al.*, 2008].

[4] Here we investigate an additional control on the distribution and area-integrated rate of ocean-driven melting: the basal slope of the ice shelf. In boundary-trapped, buoyancy-driven oceanic flow, local slope drives the

¹Department of Geosciences, Princeton University, Princeton, New Jersey, USA.

²Geophysical Fluid Dynamics Laboratory, NOAA, Princeton, New Jersey, USA.

³Woodrow Wilson School of Public and International Affairs, Princeton University, Princeton, New Jersey, USA.

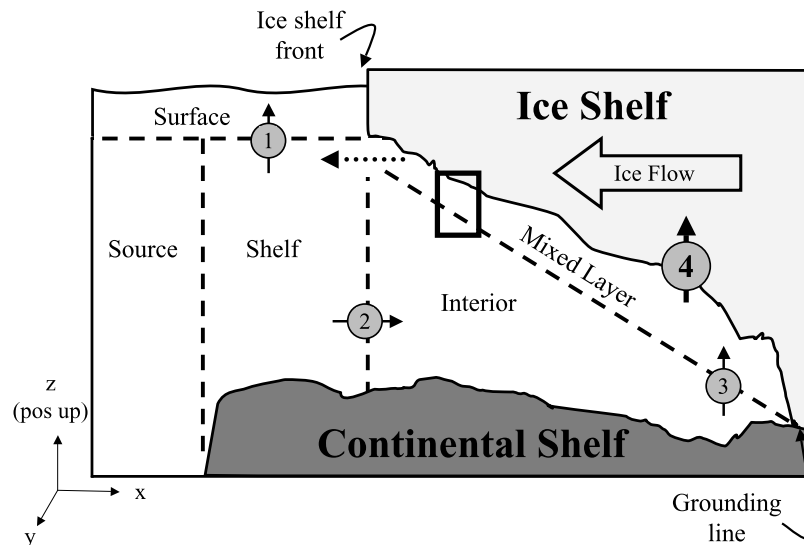


Figure 1. Key barriers (numbered arrows) in the transfer of oceanic heat to an ice shelf may be spatially segregated. The barriers illustrated schematically here are as follows: barrier 1, the base of the open-ocean mixed layer; barrier 2, the ice shelf front; barrier 3, the base of the sub-ice shelf mixed layer; and barrier 4, the ice shelf interface. Any unused heat may be advected out of the ice shelf cavity (dotted arrow). The black rectangle highlights the sub-ice shelf mixed layer subdomain, further described in Figure 2.

Richardson number down, and thus increases entrainment (mixing across stratified layers) [Ellison and Turner, 1959; Jenkins, 1991; Pedersen, 1980]. Since meltwater-freshened layers near the ice shelf base are relatively cold and stable [Nicholls et al., 2006, 2001], enhanced entrainment in regions of steeper basal slope might be expected to lead to relatively high melting rates.

[5] Observations and models of ice shelves support the importance of basal slope. Patterns of basal melting are highly nonuniform [Joughin and Padman, 2003], and there is evidence [Payne et al., 2007; Rignot and Steffen, 2008] that enhanced melting near (steep) grounding lines is characteristic of small ice shelves. Even under uniform forcing, models employing realistic ice shelf thickness gradients simulate an intensified longitudinal gradient in melting (HJH08). In coupled ice-ocean models, ice shelf thickness gradients coevolve with intensified melting near grounding lines [Grosfeld and Sandhager, 2004; Walker and Holland, 2007].

[6] The physical processes underlying the sensitivity of basal melting rates to ice shelf morphology, either in isolation or in conjunction with thermal forcing, have not been formally assessed. Here, we find that slope-dependent turbulent mixing drives high mixed layer temperatures in steep regions; the rate of ice-ocean heat transfer and the mixed layer thickness control where entrained heat is used for melting. The ratio of the entrainment rate and the ice-ocean thermal exchange velocity governs the local response to changes in slope. The distribution of melting, area-integrated melting rates, and the response to changes in ocean heat content and basal slope thus depend on ice shelf morphology. Although interaction with open-ocean dynamics adds complexity to this analysis, the glaciological control of near-ice ocean properties is likely to remain important.

[7] This paper is organized as follows: in section 1, the key barriers to heat flux and details of the numerical model are reviewed; section 2 describes the mixed layer dynamic regimes and their influence on basal melting's sensitivity to temperature and shape; and section 3 highlights the physics underlying the results, assesses the implications for glaciological and climate models, and underscores the importance of the coupled ice-ocean response.

1.1. Setting up the Physics

1.1.1. Efficiency of Basal Melting

[8] Only a fraction of the heat content of subsurface water is used to melt ice shelves; here, this fraction is termed the efficiency of basal melting. As water is advected across the continental shelf and under the ice shelf, efficiency losses can be quantified at dynamic barriers. These barriers are illustrated schematically in Figure 1: they include (1) the open-ocean mixed layer, where heat may be lost to the atmosphere; (2) the ice shelf front, where a fraction of the subsurface water is advected under the ice shelf; (3) the sub-ice shelf mixed layer, where a fraction of interior water is entrained; and (4) the ice-ocean interface, where mixed layer heat may be used to melt ice. Not all of the heat transferred to the ice shelf is used for melting; there may be conductive heat loss to the ice. This paper principally examines the efficiency of heat flux through the mixed layer; however, each barrier may influence the sensitivity of melting to open-ocean heat content.

1.1.2. Subice Mixed Layer Heat Balance: Two Barriers to Melting

[9] Insight into ice shelf-ocean heat fluxes can be gained from reduced-gravity models (i.e., with one active oceanic layer) of varying degrees of complexity [Jenkins, 1991; Payne et al., 2007]. Several dynamical processes are absent from these models, including steady flow at depth [Little

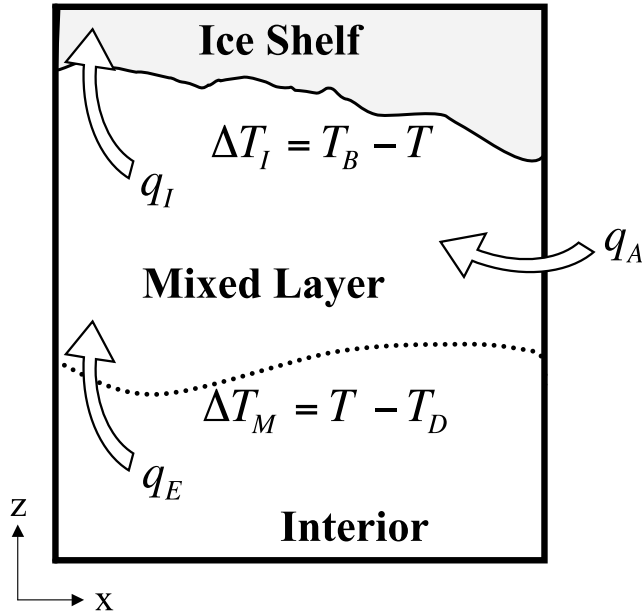


Figure 2. In the reduced-gravity and 3-D numerical models used in these experiments, oceanic heat fluxes (where q_A , q_I , and q_E are advective, ice-ocean, and entrained heat fluxes, respectively) along the longitudinal axis of an ice shelf are discretized with a bulk mixed layer. The temperature of the mixed layer (T) is bounded by the in situ freezing point (T_B) and the interior temperature (T_D).

et al., 2008] and time-dependent oceanic forcing [Makinson, 2002; Thoma *et al.*, 2008]. Yet a reduced-gravity approach is plausible for ice shelves exposed to a sluggish, relatively uniform water mass; it is also a useful introduction to the dynamics further explored with 3-D numerical simulations.

[10] In this framework, a well-mixed layer (schematically illustrated in Figure 2) is composed of interior water and meltwater. The mixed layer varies temporally and horizontally in depth, thermodynamic properties, and tracers, but is vertically homogeneous in tracers and momentum. The layer is lighter and cooler than the interior; its temperature (T) depends on the heat balance. In a steady state,

$$q_A = q_E + q_L + q_C. \quad (1)$$

The heat fluxes in equation (1) refer to advection within the mixed layer (q_A), entrainment from the motionless interior (q_E), latent cooling (q_L), and conduction into the ice shelf (q_C). Because the emphasis of this paper is on the oceanic heat balance, heat used to melt ice is defined to be negative (opposite to Q_M^T , as defined by Holland and Jenkins [1999]), and ice-ocean fluxes are aggregated; that is, $q_I = q_L + q_C$.

[11] Heat flux to the ice through a viscous sublayer may be modeled using an thermal exchange velocity, γ_T [Kader and Yaglom, 1972, 1977], such that

$$q_I = \rho_0 c_p \gamma_T \Delta T_I. \quad (2)$$

In equation (2), $\Delta T_I = T_B - T$ is the temperature difference across the sublayer, that is, between the salinity and pressure-dependent freezing point and the local mixed layer temperature, c_p is the specific heat of the mixed layer, and ρ_0 is a oceanic reference density. Various formulations for the thermal exchange velocity have been proposed, incorporating stabilizing buoyancy fluxes and molecular diffusion; yet where flow is dominantly buoyancy driven, γ_T remains a strong function of the friction velocity, u^* [Holland and Jenkins, 1999]. Observational constraints on γ_T have been gained from a limited set of measurements under sea ice [McPhee, 1992, 1999].

[12] Sublayer salt fluxes may be addressed with an analogous salinity exchange velocity (γ_S) [Mellor *et al.*, 1986]. Slow diffusion of salt through the sublayer will increase the freezing point at the ice interface relative to that of the mixed layer. For simplicity, in this section, the mixed layer–ice temperature gradient is assumed to be large relative to salinity- or pressure-dependent changes in the freezing point. Variability in the freezing point is included in the numerical simulations.

[13] Ignoring conduction and assuming a fully turbulent sublayer, the ice shelf melting rate is given by

$$m' = -\frac{\rho_0 c_p \gamma_T}{\rho_I L_f} \Delta T_I, \quad (3)$$

where ρ_I is the density of the ice shelf and L_f is the latent heat of fusion of ice. Mixed layer temperature (via ΔT_I) and flow speed (via γ_T) influence the melt rate. A positive melt rate indicates freshwater input to the mixed layer, driven by a mixed layer temperature above the in situ freezing point.

[14] Turbulent entrainment (e') across the base of the mixed layer supplies heat and salt to the mixed layer. Local shear is of primary importance, but entrainment is also influenced by stratification and nonlocal mixing processes. If tidal forcing is weak (as in the Amundsen Sea [Padman *et al.*, 2002]), shear-driven entrainment, driven by buoyant, near-ice flow, is likely to be the dominant source of mixing. To date, ice shelf–ocean models have employed an interfacial Richardson number criterion [Holland and Feltham, 2005], or a surface-stress-driven turbulent kinetic energy balance [Holland and Jenkins, 2001; Little *et al.*, 2008] to determine the rate of entrainment. Equation (1) can then be expanded:

$$\mathbf{u} \cdot \nabla(hT) = -e' \Delta T_M + \gamma_T \Delta T_I, \quad (4)$$

where $\Delta T_M = T - T_D$ is the temperature difference across the base of the mixed layer, T_D is the temperature of the interior, \mathbf{u} is the horizontal velocity, and h is the thickness of the mixed layer.

[15] Further insight into the barriers to melting can be gained by assuming that advection is negligible. In this case, a 1-D local balance holds, and equation (4) can be rewritten:

$$\frac{e'}{\gamma_T} = \frac{\Delta T_I}{\Delta T_M}. \quad (5)$$

The ice shelf does not feel the unmodified interior temperature (T_D); heat is partitioned between the mixed layer and the interior. In equation (5), the mixed layer temperature is in equilibrium (T_E) with the ice-ocean and interior–mixed layer heat fluxes [Lane-Serff, 1995]; T_E indicates the relative magnitude of γ_T and e' .

[16] In the limit of rapid latent heat flux ($\gamma_T \gg e'$), the temperature of the mixed layer approaches the freezing point; the rate of entrainment limits melting. If γ_T and e' are of the same magnitude, not all of the heat entrained into the mixed layer is transferred to the ice. Importantly, if γ_T and e' have a different dependence on physical constraints (e.g., slope), the ratio in equation (5) will vary spatially, driving horizontal gradients in mixed layer temperature and melting.

1.1.3. Defining Efficiency

[17] In this paper, sub-ice shelf (internal) control of oceanic heat is assessed at two barriers: the base of the mixed layer and the ice-ocean interface (barriers 3 and 4 in Figure 1). At each location, quantities may be defined to assess the efficiency: here, they are denoted as the entrainment efficiency (f_E) and the ice-ocean efficiency (f_I), respectively.

[18] If interior water properties are uniform and diffusive heat fluxes are negligible, the entrainment efficiency is simply the volume fraction of interior water entrained into the mixed layer. For an ice shelf with a north-south aligned front at its western boundary, in a steady state,

$$f_E = \frac{\int_{x_E}^{x_W} \int_{y_S}^{y_N} e' \partial y \partial x}{\int_{y_S}^{y_N} \int_{x_E}^{x_W} u^+(x_w) h_D(x_w) \partial x \partial y}, \quad (6)$$

where y_N , y_S , x_E , and x_W are the boundaries of the ice shelf, u^+ is the zonal velocity evaluated only where $u > 0$ (i.e., inflow), and h_D is the thickness of the interior layer.

[19] Heat entrained into the mixed layer may be used at any location along the ice shelf. This heat flux, the total available for melting, can be expressed as

$$q_T = -e' \Delta T_T, \quad (7)$$

where the overall thermal driving is $\Delta T_T = \Delta T_I + \Delta T_M = T_B - T_D$. Here, for convenience, we define q_T^{MAX} as the maximum available heat for melting, where $\Delta T_T^{MAX} = T_B^{MIN} - T_D$, and T_B^{MIN} is the minimum freezing point along the ice shelf. Because mixed layer temperatures are high, small differences in the choice of the (spatially varying) freezing point do not affect the results. Since $\Delta T_T^{MAX} > \Delta T_M$ (unless the mixed layer is supercooled), in a local balance (equation (5)), entrainment delivers more heat than that required for basal melting.

[20] Along the zonal axis of the ice shelf, assuming the mixed layer flows upslope, the excess heat flux (H_X) is

$$H_X(x) = \int_{x_E}^x (Q_T^{MAX} + Q_I) \partial x, \quad (8)$$

where meridionally integrated heat fluxes are given in capital letters. The gradient of excess heat along the ice shelf is

$$\frac{dH_X}{dx}(x) = (Q_T^{MAX} + Q_I). \quad (9)$$

Integrated over the ice shelf, the fraction of entrained heat used for melting (the ice-ocean efficiency) is

$$f_I(x_w) = \left[1 - \frac{H_X(x_w)}{\int_{x_E}^{x_W} \int_{y_S}^{y_N} Q_T^{MAX} \partial y \partial x} \right], \quad (10)$$

and the overall efficiency of melting (f_O) is

$$f_O = f_E f_I(x_w). \quad (11)$$

In subsequent sections, we use a numerical model to examine the magnitude and spatial distribution of mixed layer heat fluxes, which influence the efficiency of melting and its sensitivity to ice shelf morphology and ocean temperature.

1.2. Numerical Model

[21] Simulations were performed with the Hallberg Isopycnal Model [Hallberg and Gnanadesikan, 2006], a Boussinesq, 3-D, numerical ocean model. The model incorporates the barriers to heat transfer (barriers 3 and 4 in Figure 1) using a bulk mixed layer [Hallberg, 2003] and a thermodynamic parameterization of ice-ocean fluxes [Little et al., 2008] (after the three-equation formulation of Holland and Jenkins [1999]). A local turbulent kinetic energy (TKE) balance determines the rate of entrainment. The mixed layer shoals in response to ice shelf melting and deepens with increasing shear, scaling with the Monin-Obhukhov length scale [Niiler and Kraus, 1977]. Shear production of TKE is calculated using a quadratic drag law employing a spatially and temporally fixed drag coefficient of 2.5×10^{-3} . Interior and nonlocal mixing may be addressed using additional parameterizations [Hallberg, 2000; Jackson et al., 2008]; given the limited vertical resolution, these were not included in these simulations.

[22] The morphological details of ice shelves vary owing to local bedrock topography and embayment shape, which modify the stress balance and thus the ice shelf thickness and flow rate. Spatially comprehensive, accurate ice thickness measurements are difficult to obtain without concerted effort [Corr et al., 2002]. Yet it is known that the aspect ratio of ice shelves, even within the Amundsen Sea, varies considerably; from confined, narrow, deep ice shelves (Pine Island Ice Shelf, or PIIS, $\sim 2300 \text{ km}^2$) to large ice shelves covering multiple embayments (Getz Ice Shelf, $> 30,000 \text{ km}^2$) [Shepherd et al., 2004]. These ice shelves exhibit strong longitudinal (along-ice flow) thickness gradients; near grounding lines, basal slope may be an order of magnitude larger than tens of kilometers down-glacier [Corr et al., 2001].

[23] In the numerical simulations, the principal configuration (BASE) aims to reproduce key large-scale aspects of PIIS; it features a zonally uniform bathymetric trough (maximum depth 900 m) that is intersected by a meridionally

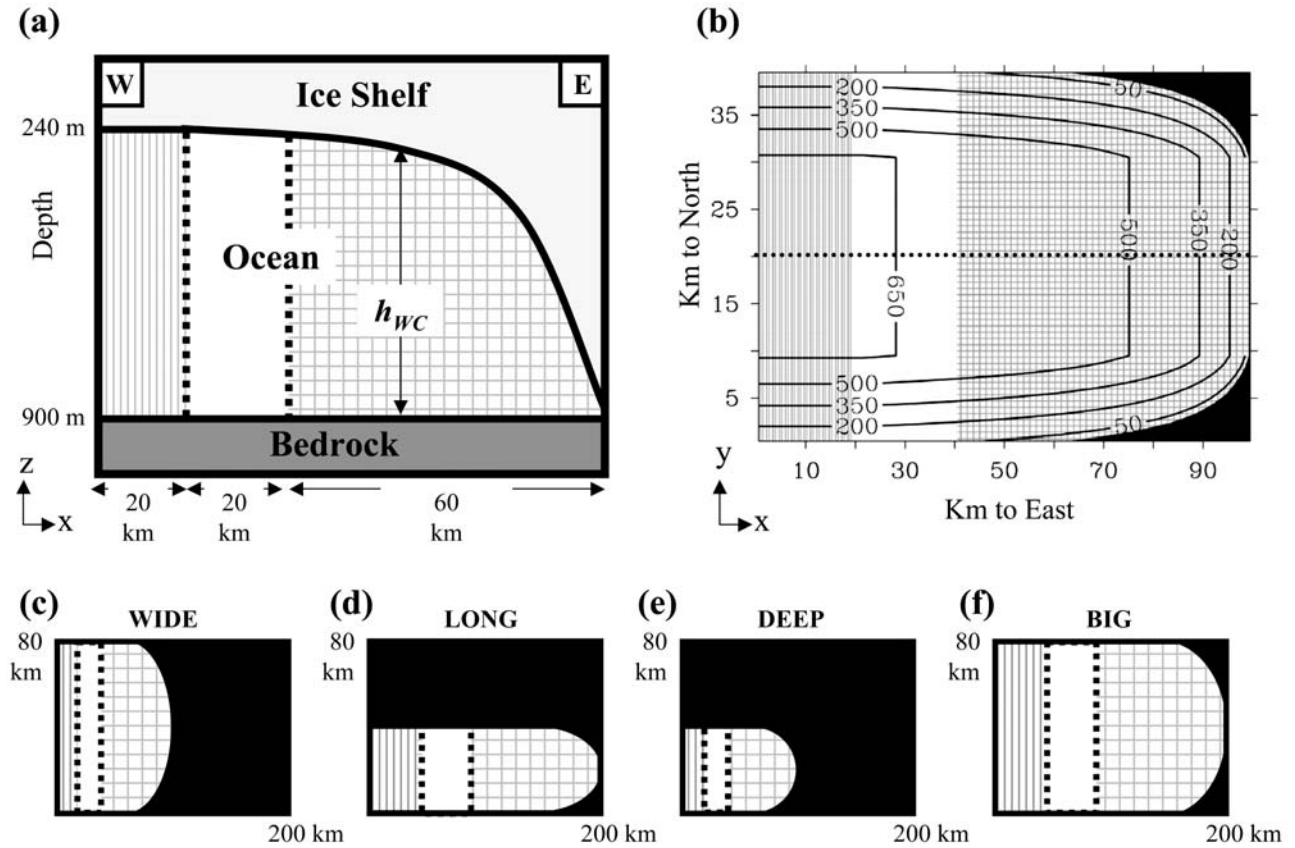


Figure 3. Schematic (a) cross-section and (b) map views of the principal configuration (BASE) employed in these simulations. Figure 3a depicts the ice shelf draft at $y = 20$ km. Contours in Figure 3b indicate the water column thickness (h_{WC}); the dotted line is the location of Figure 3a. (c–f) Alternate ice shelf configurations (further described in Table 1). Vertical shading indicates the portion of the domain where interface heights, temperature, and salinity are restored to their initial conditions. Analysis of the simulations is performed only on the easternmost 3/5 of the model domain (hatched regions), limiting the influence of the applied restoring.

uniform ice shelf (Figures 3a and 3b). The depth of the ice shelf base (B) as a function of distance to the east (x , in m) is described by

$$B = \min \left\{ 240, \frac{\alpha_1}{(\alpha_2 - \frac{x}{1000})^{25}} \right\}, \quad (12)$$

where $\alpha_1 = 2200$ and $\alpha_2 = 106$.

[24] The slope of the BASE case thus varies from 0.06 at the deepest location in the domain ($x = 100$ km) to near zero at 20 km. This shape is smaller and steeper than those used in other idealized studies [HJH08; Walker *et al.*, 2008], and defines a grounding line that circumscribes the ice shelf cavity. To illuminate slope- and scale-driven control of basal melting, alternate ice shelf aspect ratios are examined (described in Table 1 and Figures 3c–3f). In all configurations, the minimum water column thickness is 10 m.

[25] All simulations are initialized with a 10 m thick mixed layer at the in situ freezing point and an interior layer initialized at a fixed temperature (T_D) that varies between -2.0°C to 1.5°C across simulations; the salinity of the interior is always 34.9 practical salinity units (psu). Layer interfaces and properties are restored to initial values over

the western 1/5 of the model domain. To mitigate any effects of the applied restoring, only the eastern 3/5 of the domain is analyzed (the “analysis region”). Buoyancy-driven flow and tracer properties are allowed to evolve over 60 days. In all model runs, basal melting rates and kinetic energy stabilize after ~ 20 days, and all output discussed in this paper reflects quantities averaged over the final day of the simulation.

[26] The ice shelf is nondynamic, implying a steady local mass balance. Heat conduction into the ice is described by

Table 1. Details of Alternate Ice Shelf Configurations^a

	W (km)	L (km)	A (10^3 km ²)	D (m)	θ_{max} (10^{-2})	$\bar{\theta}_O$ (10^{-2})	$\bar{\theta}_I$ (10^{-2})
BASE	40	60	2.2	900	6.4	0.88	4.4
WIDE	80	60	4.4	900	6.4	0.88	4.4
LONG	40	120	4.6	900	6.4	0.42	4.4
DEEP	40	60	2.3	1200	8.6	1.21	5.9
BIG	80	120	8.7	900	3.2	0.44	2.9

^a W , L , and D are the maximum width, length, and depth of each ice shelf cavity. A is the area of the ice shelf base. The basal slope is averaged over the entire analysis region and the initiation (westernmost 5 km) region (O and I subscripts, respectively). All dimensions are for the analysis region of each simulation.

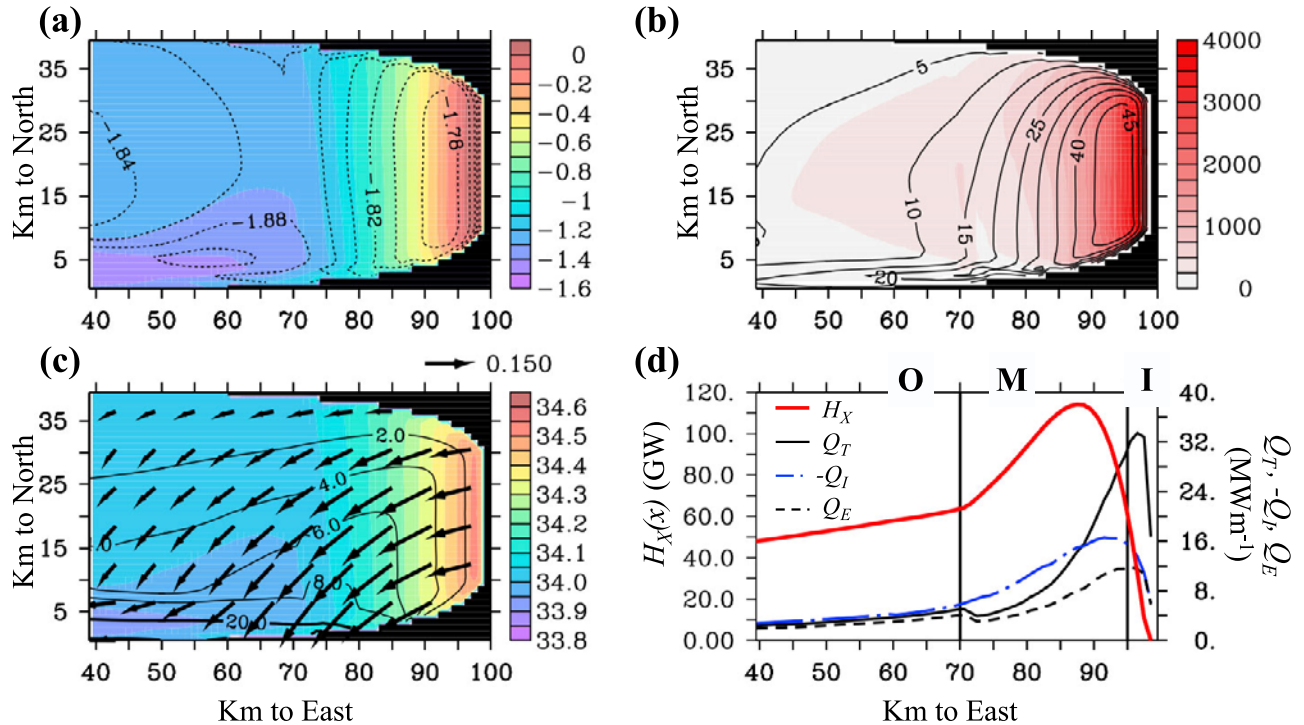


Figure 4. Steady state mixed layer properties in the eastern 60 km of the BASE case ($T_D = 1.0^\circ\text{C}$) are forced by strong spatial gradients in heat fluxes. (a) The mixed layer temperature (T , $^\circ\text{C}$, shading) and in situ freezing point (T_B , $^\circ\text{C}$, contours). (b) The entrainment rate (e' , m yr^{-1} , shading) and ice shelf melting rate (m' , m yr^{-1} , contours). (c) The mixed layer salinity (S , practical salinity units (psu), shading), thickness (h , m , contours), and velocity (\mathbf{u} , ms^{-1} , vectors). (d) Meridionally integrated heat fluxes ($-Q_I$, the heat flux to the ice; Q_T , the entrained heat flux relative to the freezing point; and Q_E , the entrained heat flux) plotted against the right-hand axis. The excess heat flux (H_X) is overlain as a thick red line against the left-hand axis. Vertical lines indicate the initiation (I), maintenance (M), and outflow (O) regions.

an advective/diffusive heat balance [Holland and Jenkins, 1999]; the interior ice temperature is assumed to be -15°C . No ice shelf front or open ocean is included; simulations with a portion of the domain outside of the ice shelf cavity did not change the nature of the results.

2. Results

[27] Oceanic heat initiates differential melting that, when coupled to the circulation, establishes the steady state mixed layer hydrography, flow, and heat fluxes illustrated for the BASE case ($T_D = 1.0^\circ\text{C}$) in Figures 4a–4c. Gradients in ΔT_I are driven by ocean temperature, rather than the in situ freezing point, which varies little underneath the ice shelf; salinity-dependent changes in the freezing point compensate for its pressure dependence. Temperatures are highest near the grounding line, reaching a maximum of 0.1°C ($\Delta T_I^{\text{max}} = 1.93^\circ\text{C}$). Since the mixed layer is comprised solely of interior water and ice shelf meltwater, salinity gradients are proportional to those of temperature [Gade, 1979]. Though the meltwater fraction by volume is relatively small (≤ 25 ppt), especially near cavity boundaries, melting cools and freshens the mixed layer; the addition of buoyancy drives a southwestward frictional-geostrophic flow [Price and Baringer, 1994]. Mixed layer thicknesses are generally less than 10 m, with regions near boundaries less than 2 m. There is little meridional (transverse to the

ice flow) variation in oceanic properties or melting rates, except adjacent to the southern boundary, where flow converges.

[28] High mixed layer temperatures coincide with maximal rates of entrainment ($e' \sim 4000 \text{ m yr}^{-1}$) of interior water. Despite ongoing entrainment of heat, the mixed layer cools as it flows upslope, reaching -1.4°C approximately 30 km from the grounding line. Along flow paths, temperature decreases monotonically; the velocity profile is more complex. Two factors contribute to the relatively constant flow speed ($\sim 0.20 \text{ ms}^{-1}$) over the western 30 km of the domain: (1) As meltwater accumulates upslope, density and slope-driven contributions to the pressure gradient compensate; and (2) near the deepest part of the ice shelf, frictional drag is larger, owing to the thin mixed layer. Flow speed and turbulent mixing are coupled, increasing in tandem until decreasing slope acts to weaken the pressure gradient. As a result of the spatial decorrelation of temperature and velocity, melting rates, driven by the product of these properties (equation (3)), are maximized over a broad region approximately 5–10 km from the grounding line. The maximum melting rate is 49 m yr^{-1} ; it is shifted upslope of the entrainment maximum.

2.1. Mixed Layer Dynamic Regimes

[29] To examine these strong zonal gradients in mixed layer temperature and salinity, it is useful to divide the

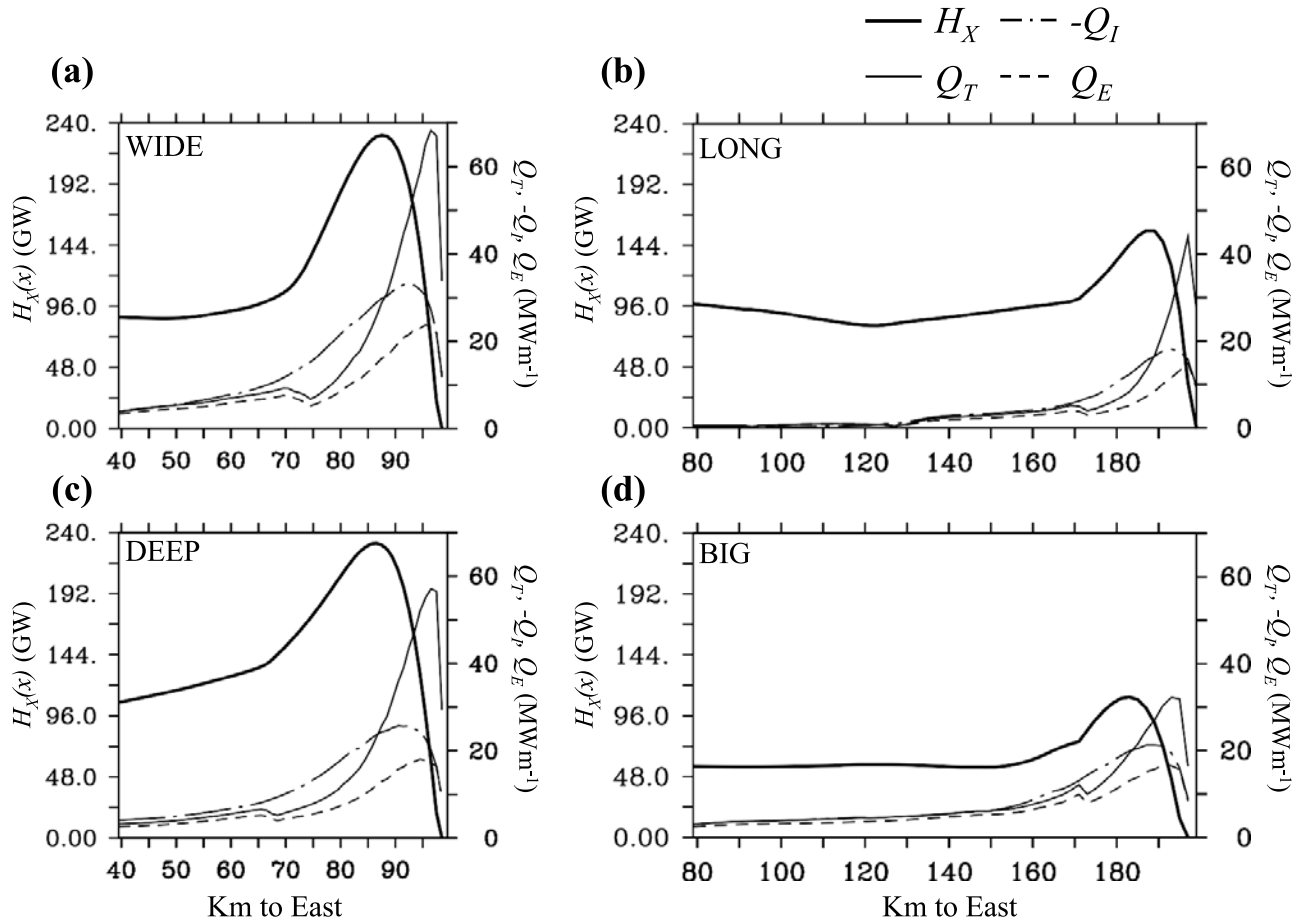


Figure 5. (a–d) Mixed layer heat fluxes for alternate configurations indicate that distinct mixed layer regimes and inefficiency are pervasive features. Meridionally integrated heat fluxes ($-Q_I$, the heat flux to the ice; Q_T , the heat flux relative to the freezing point; and Q_E , the entrained heat flux) are plotted against the right-hand axis. The excess heat (H_X) is overlain as a thick line against the left-hand axis. The interior temperature (T_D) in each plot is 1.0°C .

cavity into three regions: the “initiation” region, here, defined to be within 5 km of the deepest point of the ice shelf; the “maintenance” region, between 70 and 95 km; and the “outflow” region, west of 70 km. The regions are differentiated by their heat balance (Figure 4d): slope-driven changes in the rate of entrainment, flow speed, and mixed layer thickness control local temperature and importance of advection. Although these regimes share characteristics with those described by Lane-Serff [1995], the mixed layer dynamics in these 3-D simulations differ.

[30] In the initiation region, the flux of heat available for melting (Q_T) rapidly increases to several times larger than the ice-ocean heat flux (Q_I), driving high mixed layer temperatures (T) and rapid accumulation of heat (H_X). Here, where a local heat balance (equation (5)) is applicable, the partitioning of the ice-interior temperature gradient ($\Delta T_T^{900\text{m}} \sim -3.3^\circ\text{C}$, $\Delta T_I^{900\text{m}} \sim -1.9^\circ\text{C}$) indicates that e' exceeds γ_T .

[31] In the maintenance region, Q_T decreases rapidly; advection ($Q_A = Q_I + Q_E$) weakens horizontal temperature gradients driven by the shape of the ice shelf. Since a nonnegligible advective heat flux is maintained, the heat balance is better described by equation (4). Including

nonlocal contributions to the heat balance increases ΔT_I relative to equation (5) (i.e., $T > T_E$); ice-ocean heat flux (Q_I) increases in proportion to the advected anomaly, $T - T_E$, cooling the mixed layer. As seawater rises along the (thinning) ice shelf, decreasing entrainment acts to increase Q_I relative to Q_T ; mixed layer cooling opposes this tendency. The transition between accumulation and use of heat (where $Q_T = -Q_I$ and $\partial H_X / \partial x = 0$) occurs approximately 15 km from the grounding line in the BASE configuration; it is controlled by local slope (which drives e' / γ_T) and the upstream morphology (which controls advected heat, and thus gives $\Delta T_I / \Delta T_T$).

[32] In the outflow, Q_I exceeds Q_E , but heat fluxes are greatly reduced compared to regions of higher slope. The decay of excess heat ($\partial H_X / \partial x$) decreases sharply as southward flow converges; even though the mixed layer temperature is higher than a local heat balance dictates, it relaxes only slowly toward the freezing point. In the BASE simulation, Q_I exceeds Q_E along the entire extent of the maintenance and outflow regions; the decay of excess heat is incomplete. In aggregate, these regimes conspire to trap previously entrained heat in the mixed layer (which exits the analysis region at approximately -1.5°C , well above the

Table 2. Summary of Temperature and Shape Sensitivity Analysis^a

Simulation	\bar{m}'_O	\bar{m}'_I	\bar{m}'_{max}	$ x_{75\%} $	f_M	f_E
BASE						
-1.5	1.20	5.92	4.63	0.35	0.95	0.24
-0.5	5.49	19.87	15.30	0.44	0.90	0.25
0.5	11.90	38.45	29.61	0.47	0.89	0.26
1.5	21.03	60.29	46.61	0.54	0.87	0.24
WIDE						
-1.5	1.15	5.99	4.67	0.31	0.97	0.23
-0.5	5.43	19.95	15.38	0.42	0.94	0.25
0.5	11.95	38.42	29.71	0.46	0.92	0.26
1.5	20.40	60.49	46.95	0.50	0.91	0.29
LONG						
-1.5	0.65	6.76	5.49	0.18	0.92	0.27
-0.5	2.99	22.47	17.96	0.24	0.89	0.43
0.5	6.55	43.82	34.73	0.27	0.86	0.36
1.5	11.50	69.43	54.82	0.31	0.85	0.54
DEEP						
-1.5	2.31	10.02	7.84	0.36	1.01	0.39
-0.5	9.08	29.47	22.51	0.45	0.96	0.34
0.5	18.94	54.81	41.61	0.49	0.94	0.33
1.5	31.75	84.73	64.13	0.52	0.93	0.29
BIG						
-1.5	0.56	4.23	2.81	0.26	0.92	0.15
-0.5	2.58	13.77	8.92	0.33	0.86	0.22
0.5	5.92	26.39	17.00	0.40	0.85	0.26
1.5	10.94	41.56	26.47	0.52	0.84	0.30

^aThe melting rate (m' , in $m\ yr^{-1}$) is averaged over the entire analysis region and the initiation (westernmost 5 km) region (O and I subscripts, respectively). $|x_{75\%}|$ is the fraction of the analysis region over which 75% of the melting (integrated from the eastern boundary) occurs. For example, in the BASE, -1.5°C , simulation, 75% of basal melting occurs in the eastern 35% of the ice shelf.

local freezing point), so that the area-integrated ice-ocean efficiency (f_i) is 87%.

2.2. Shape and Temperature Sensitivity

[33] Changes in the interior temperature, aspect ratio, or the area of the ice shelf do not change the nature of the three regimes (Figure 5). Meridional variability remains weak; changes in the ice shelf aspect ratio add more, longer, or steeper flow paths along the ice shelf base. The results obtained for alternate forcing and shape scenarios are summarized in Table 2; they indicate that ice shelf slope controls the entrainment of heat, the efficiency with which it is used, and the distribution of basal melting.

[34] In all simulations, melting is concentrated in the deeper parts of the ice shelf. This local enhancement of melting occurs despite a smaller meridional extent of the ice shelf in these regions. Maximum melting rates (m'_{MAX}), always located near the deepest part of the ice shelf, are 2.6 to 10.3 times higher than melting rates (\bar{m}'_O) averaged over the analysis region. A more realistic representation of stratification (a cooler, fresher upper water column) would likely enhance this gradient.

[35] Steeper ice shelves have a higher mean melting rate; area-averaged power laws of the form $\bar{m}'_O = c\theta^n$ give an exponent of 0.94 to 1.15 (dependent on the interior temperature). However, basal melting's sensitivity to slope is hidden by spatial inhomogeneity (Figure 6). In the initiation region, slope-dependent basal melting power laws ($\bar{m}'_I = c\theta^n$) give an exponent of 1.21 to 1.37 (for each interior temperature, the exponent is larger in the initiation region than the analysis region).

[36] All configurations show a common, superlinear response to increasing ocean temperature, although the exact dependence differs; the details of morphology influence the response to temperature (Figure 7). Area-averaged melting rates obtained over a temperature range $-2.0^\circ\text{C} \leq T_D \leq 1.5^\circ\text{C}$ show negative deviations from a quadratic scaling – which is consistent with earlier numerical studies (HJH08). Power laws of the form $\bar{m}'_O = c(\Delta T_I)^n$ give an exponent of 1.55 to 1.81.

[37] The slope dependence of entrainment is more pronounced than that of melting, driving increases in advected heat; as temperature and slope in the initiation region increase, f_i declines and distribution of melting shifts seaward. Advective heat loss increases steadily with thermal driving for all cavity shapes (shown for the BASE case in Figure 8). Incomplete cooling drives a decrease in ice-ocean efficiency, driving divergence from a quadratic scaling.

[38] In these simulations, the efficiency of entrainment (f_E) is always below 55%, indicating a significant amount of heat is recirculated underneath the ice shelf, however, it does not exhibit strong trends with temperature or ice shelf shape.

3. Discussion

[39] These results indicate that ice shelf basal slope controls the entrainment of heat into the mixed layer. However, they indicate that the processes controlling how this heat is transferred to the ice may complicate simple melting/slope and melting/interior temperature scaling laws. The underlying physics, as well as their implications for modeling and observational efforts, are discussed below.

3.1. Local Slope Dependence of the Melting Rate

[40] The slope dependence of turbulent entrainment may be examined using energetic considerations. Mechanical energy derived from surface stress at the ice interface mixes the local meltwater flux and entrained interior water [after *Niiler and Kraus, 1977*]:

$$\frac{u_*^3}{\kappa} = \frac{h}{2}(B_0 - \beta g' \Delta S_M), \quad (13)$$

where u_* is the friction velocity (ms^{-1}), h is the thickness of the mixed layer (m), κ is Von Karman's constant, g' is the acceleration due to gravity (ms^{-2}), β is the salinity contraction coefficient, $\Delta S_M = S - S_D$ is the salinity difference across the base of the mixed layer, S_D is the salinity of the interior (psu), and B_0 is the buoyancy flux at the ice-ocean interface (m^2s^{-3}). Ignoring thermal expansion and meltwater input, the buoyancy flux is given by

$$B_0 \approx -\beta g m' S. \quad (14)$$

The local salt balance in the mixed layer is

$$e' = \frac{m' S}{\Delta S_M}. \quad (15)$$

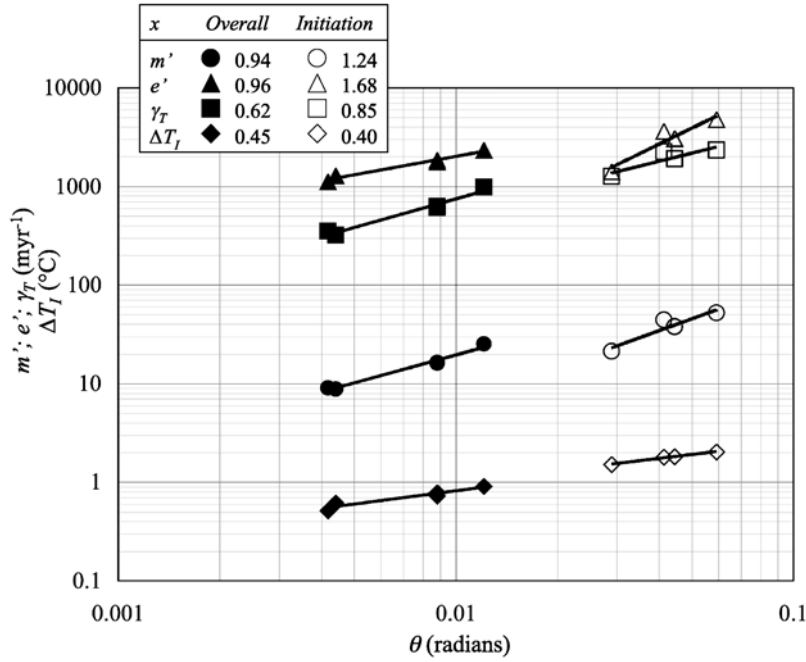


Figure 6. Mixed layer heat fluxes exhibit different dependence on local slope, and their sensitivity to slope is a function of the area over which quantities are averaged. In the legend, the values of γ_T (the ice-ocean transfer velocity), e' (the mixed layer entrainment rate), m' (the melting rate), and ΔT_I (the ice–mixed layer temperature gradient) are spatially averaged over the analysis region (“overall,” in solid symbols) and the first 5 km (“initiation,” in open symbols) for all configurations employed in these experiments ($T_D = 1.0^\circ\text{C}$). The trend lines shown are for power laws of the form $x = c\theta^n$, where the exponent n is noted in the legend.

Combining equations (13)–(15), we get

$$\frac{u_*^3}{\beta\kappa gh} \approx e' \Delta S_M. \quad (16)$$

Scaling equation (16), letting $u_* \sim U \sim \Delta S \sin \theta \sim \Delta S \theta$, where θ is the angle if the ice shelf’s lower surface with respect to a geopotential surface, we get

$$E \sim \frac{\Delta S^2 \theta^3}{H}. \quad (17)$$

A scaling for H must be consistent with mass conservation; that is,

$$E \sim \frac{UH}{L}, \quad (18)$$

suggesting that $H \sim U$ and $E \sim U$. This dependence is captured in the simple form for entrainment [Pedersen, 1980] employed by HJH08 and Jenkins [1991]:

$$e' = c_E |u| \sin \theta, \quad (19)$$

where c_E is an empirical constant; it is also consistent with a Richardson number scaling: in a buoyancy-driven current, for any density gradient, flow speed increases with slope.

[41] In the BASE simulation, e' is poorly predicted by flow speed (Figure 9a), but improves upon introducing the

local slope (Figure 9b), implying that the form of equation (19) is adequate. Using equations (3), (5), and (19), the control of mixed layer temperature and melting rates can be expressed in terms of the overall thermal driving (ΔT_I):

$$\Delta T_I = \left(\frac{\gamma_T}{e'} + 1 \right)^{-1} \Delta T_T, \quad (20)$$

$$m' \propto \frac{\gamma_T e'}{\gamma_T + e'} \Delta T_T. \quad (21)$$

The magnitude of e' and γ_T determines the sensitivity to slope. Although e'/γ_T varies over the ice shelf, numerical simulations indicate that this ratio is $O(1)$ over most of the domain. Assuming $U \sim \theta$, and using equation (19), $\gamma_T \sim \theta$ and $e' \sim \theta^2$. A scaling for mixed layer temperature and melting rate in a local heat balance is then given by

$$T \sim \frac{\theta}{1 + \theta}, \quad (22)$$

$$m' \sim \frac{\theta^2}{1 + \theta}. \quad (23)$$

In Figure 6, e' approaches a quadratic dependence with slope (expected if $U \sim \Delta S \theta$), while γ_T shows a slight negative departure from linearity [Holland and Jenkins, 1999]. As predicted by equation (23), the numerical model

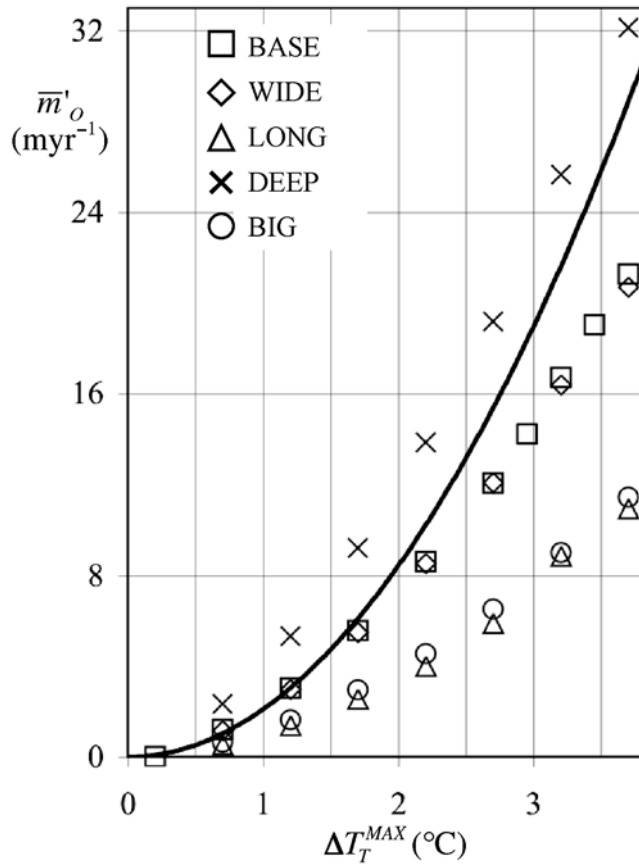


Figure 7. Melting rates are uniformly higher as interior temperature increases, but decreases in ice-ocean efficiency drive a departure of the area-averaged melting rates (\bar{m}'_O , m yr^{-1}) from a quadratic dependence on thermal driving (ΔT_T^{MAX}) for all ice shelf configurations. A quadratic extrapolation of the BASE case melt rate based on the increase from 0°C to 1°C of thermal driving is included (black solid line) for comparison.

confirms a slope dependence of basal melting intermediate between that of e' and γ_T ; mixed layer temperature exhibits a weaker dependence, as predicted by equation (22).

[42] These simulations suggest that the parameterization of entrainment is important in large-scale models, especially the nature of its divergence from the ice-ocean exchange velocity. Though buoyancy fluxes affect this ratio, they drive e' and γ_T in the same direction. Slope should be expected to drive large variations in equation (5); even weak dependence will drive substantial spatial variability under realistically shaped ice shelves.

3.2. Role of Advection and Efficiency

[43] The presence of subsurface meltwater-freshened water masses substantially above the surface freezing point near ice shelves in the Bellingshausen [Jenkins and Jacobs, 2008] and Amundsen [Jacobs et al., 1996] Seas suggests that heat near the ice-ocean interface is unused. The simulations described here indicate that this inefficiency is driven by the slow decay rate of advected thermal anomalies ($T-T_E$) originating in regions of higher slope.

[44] The temperature of outflow (-1.5°C) is insensitive to ice shelf shape; ice-ocean heat flux is controlled primarily

by the thickness of the mixed layer, rather than the distance traveled along the ice shelf base. A minimum decay length scale for excess heat can be examined by assuming that (1) the relatively small meltwater fraction does not change the volume or temperature of the plume, (2) T_B , h , and basal slope are constant along the ice shelf, and (3) a constant drag coefficient and a weak dependence of γ_T on buoyancy flux (HJH08); that is,

$$\gamma_T = g_T |u|, \quad (24)$$

where $|u|$ is the flow speed and g_T is a constant transfer velocity. Equation (4) may then be rewritten:

$$\frac{dT}{ds} = \frac{1}{h} (g_T \Delta T_I - c_E \Delta T_M), \quad (25)$$

where c_E is a constant that includes the (constant) slope. In equation (25), a thermal anomaly will decay toward T_E with an e -folding length scale that is solely a function of the layer thickness and the transfer velocity. For $c_E = g_T = 4 \times 10^{-4}$ and $2 < h < 10$ m, the initial thermal forcing decays exponentially over 40 to 200 km, indicating that advective heat loss is likely.

[45] Mixed layer cooling is slowed further by downstream convergence. Using a 2-D plume model, Lane-Serff [1995] observed that the layer thickness along the flow path of an entraining plume controls its dependence on the ice-ocean heat flux: a thicker layer decreases the cooling rate. Here, in 3-D simulations, horizontal flow convergence drives the retention of mixed layer heat. Since the frictional-geostrophic current in this simulation flows southwest (Figure 4b), with an upslope turning angle dependent on frictional drag, the southern boundary traps the buoyant

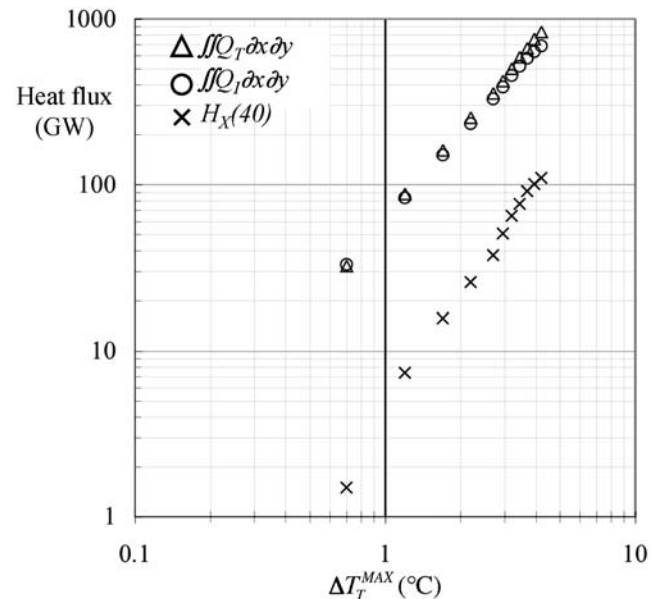


Figure 8. Area-integrated ice-ocean (circles) and entrained heat fluxes diverge with increasing thermal driving in the BASE case. The difference between these two heat fluxes is approximately equal to the heat exported from the ice shelf cavity, shown with crosses.

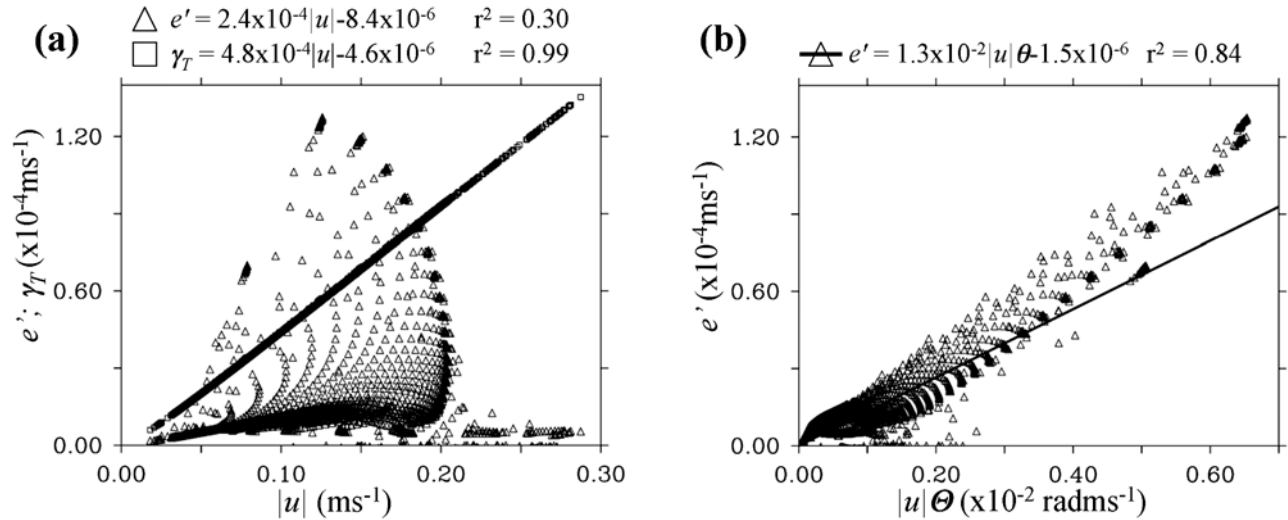


Figure 9. Regressions of e' and γ_T against (a) flow speed ($|u|$) and (b) $|u|\theta$ (e' only) indicates that entrained heat is strongly governed by basal slope. In Figures 9a and 9b, each grid point in the analysis region of the BASE simulation ($T_D = 1.0^\circ\text{C}$) is plotted. In Figure 9a, γ_T shows only a slight departure from linearity with flow speed. Entrainment is clearly a nonlinear function of flow velocity; including slope (Figure 9b) improves the regression dramatically, but e' remains systematically higher at high slopes.

outflow. If there is no entrainment or detrainment from the mixed layer, mass is conserved in the boundary current:

$$\frac{VH_M}{L_M} \sim \frac{UH_O}{L_O}. \quad (26)$$

Scales for velocity, layer thickness, and the width of the maintenance region are given by V , H_M , and L_M , respectively; those for the outflow region are given by U , H_O , and L_O . Velocity scales can be derived for boundary currents and geostrophic flow, but are functions of slope, which varies greatly in these experiments. In Figure 4c, flow speed in the outflow and maintenance regions are similar. Assuming U and V are equivalent in equation (26), the thickness of the outflow is determined by the relative widths of the boundary current and the ice shelf. The width of outflowing boundary currents under ice shelves are governed by dynamics explored by Little *et al.* [2008]; they are likely to be narrower than ice shelves, forcing convergence.

[46] With the simplified morphology employed here, side boundaries cause convergent flow, however, smaller-scale subice basal features (channels) may also act to channel outflow; the relevance of the outflow dynamics may not be limited to simplified domains. The importance of flow convergence to melting rates and distributions implies that a 2-D (x - z) approach along the ice shelf flow may be limited, even in the absence of small-scale features.

3.3. How Efficiency Affects Basal Melting's Sensitivity to Temperature

[47] The zonal distribution of heat fluxes in the BASE case (Figure 10a) indicates that entrained heat in the initiation and maintenance regions increases with interior temperature, yet a substantial fraction is unused. If a mixed layer with an initial thermal anomaly flows along the ice

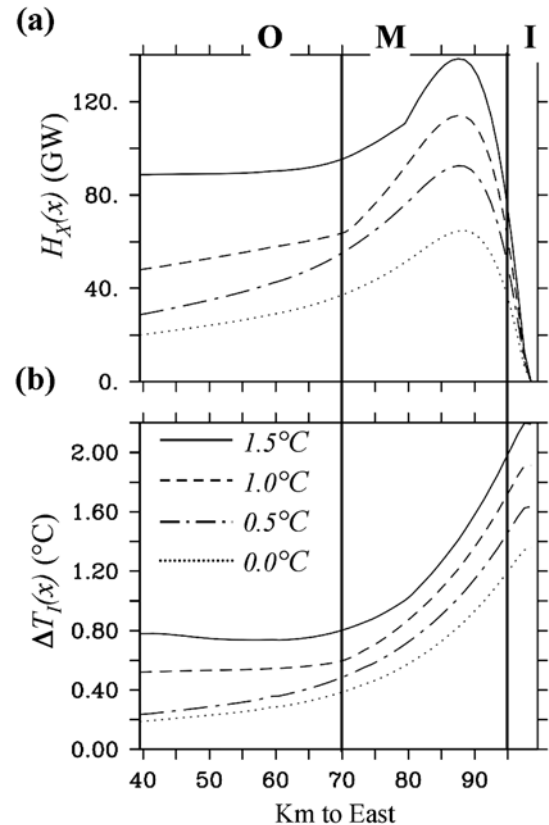


Figure 10. The meridionally averaged (a) excess heat (H_X) and (b) ice-ocean temperature gradient (ΔT_I), shown for four interior temperatures ($0.0^\circ\text{C} < T_D < 1.5^\circ\text{C}$), reveals accumulation of heat not compensated by downstream cooling. Vertical lines separate the initiation (I), maintenance (M), and outflow (O) regions.

shelf without further entrainment, equation (25) can be integrated to describe the temperature along a flow path:

$$T(x) = [T_0 - T_E]e^{-\frac{(c_E + \gamma_T)}{h}x} + T_E. \quad (27)$$

Defining ΔT as the temperature drop across the region of advective influence, and T_0 as the maximum mixed layer temperature attained in the initiation region (assumed to be in a local heat balance, where $T_0 \sim T_D$), we get

$$\Delta T \sim \Delta T_D e^{-\frac{\gamma_T}{h}x}. \quad (28)$$

Where advective heat flux is nonnegligible, the local thermal response to sub-ice shelf warming is a fraction of the increase in the initiation region: cooling occurs gradually over the ice shelf. If mixed layer dynamics do not change dramatically with interior temperature, some of the increase in entrained heat remains in the mixed layer as it escapes the ice shelf. Meridionally averaged temperature profiles from the numerical results (Figure 10b) support this simple analysis: the local response is constant over the range in interior temperature, and the temperature of the mixed layer at the ice shelf front increases by 0.6°C over a 1.5°C range in T_D .

[48] In a simplified set of equations describing the sensitivity of basal melting to ocean temperature, HJH08 assumes all heat in the well-mixed layer beneath the ice shelf is used for melting ($f_I = 1$). When melting is limited by ice-ocean heat flux (γ_T), a scaling law based on entrainment will not be valid. Only a fraction of entrained heat is used. Because this fraction decreases with temperature, area-integrated melting and entrainment exhibit a differing sensitivity to ocean thermal forcing.

3.4. Implications for Simple Models and Parameterizations of Basal Melting

[49] The slope-dependent dynamics explored here may inform efforts to develop simple models that represent (1) patterns of basal melting along the longitudinal axis of an ice shelf [Walker *et al.*, 2008] and (2) aggregated ice-ocean heat and freshwater fluxes [Beckmann and Goosse, 2003]. Although the principal configuration and oceanographic conditions examined here were chosen with reference to the Amundsen Sea, the large range of thermal forcing and shapes employed in the numerical simulations imply that these findings may be more broadly applicable.

[50] For glaciological considerations, sharp, slope-driven, spatial gradients in temperature, velocity, and melting imply that an area-averaged representation will not adequately characterize basal melting (or its response to climate). Since much of the ice shelf contributes very little to basal melting, efforts should focus on characterizing the physical processes responsible for melting deeper, steeper portions of the ice shelf.

[51] Yet even over subsections of the ice shelf, developing a generalized relationship that accounts for spatial variable dynamics poses difficulties. As the majority of ice shelf melting in these simulations occurs in the maintenance region, accounting for nonlocal heat sources may be required to estimate the longitudinal distribution of melting. Additionally, the local melting rate is a function of both the thermal forcing and the flow speed (equation (3)). Simple

basal melting models require spatially correlated rates of increase for these variables. Prior efforts to develop scaling laws have used a meltwater-dependent geostrophic approximation to account for flow speed. However, these simulations do not show a clear salinity-flow speed relationship, owing to the spatially varying slope and frictional effects in thin mixed layers and near side boundaries.

[52] Ignoring advective heat fluxes, the simplest model for temperature and basal melting (equations (20)–(23)) requires a functional form for e' and γ_T that captures their slope dependence and relative magnitudes, underscoring the need for observational validation of these parameters.

[53] The distribution of melting under an ice shelf may be less relevant for large-scale climate modeling, in which integrated ocean-cryosphere heat and freshwater fluxes are paramount. Yet the strong slope dependence of entrainment, melting, and ice-ocean efficiency influences these integrated quantities. In these simulations, integrated heat fluxes are more dependent upon the local response to slope than changes in efficiency, but the absolute magnitude of each effect will depend strongly on oceanographic conditions and the details of the ice shelf shape. At a minimum, these findings suggest that models seeking to connect far-field subsurface ocean temperatures to aggregate basal melting rates should account for the gradient in basal slope muted by an efficiency factor that is dictated by the large-scale morphology and thermal forcing.

[54] This paper demonstrates that ice shelf shape and subsurface temperature control melting rates; in fact, they are interdependent. This poses difficulties for the development of simple scaling relationships on an integrated basis, that is, of the form

$$m' = f_O \theta^{n_\theta} \Delta T_T^{n_T}, \quad (29)$$

where f_O is an ice shelf efficiency factor, n_θ is the sensitivity to slope, and n_T is the sensitivity to temperature. Because these exponents are functions of the ice-ocean efficiency, melting may have a complex dependence on morphology and oceanographic conditions. Additionally, these results do not indicate a consistent relationship between integrated melting rates and overall efficiency. As temperature and shape are changed, changes in the entrainment efficiency (f_E) and the import of heat into the ice shelf are nonlinear; additional heat for melting is not derived exclusively from either. Since the heat flux into the ice shelf cavity in these simulations is a slave to the buoyancy forcing (i.e., an infinite heat reservoir), a detailed investigation of the dynamics controlling heat flux at the ice shelf front is not possible. The interaction of internal efficiency, the coupled melting/inflow response, and external heat sources deserves further investigation.

[55] Perhaps more promising than the development of a precise scaling law are studies that investigate the magnitude and timescale of the glaciological response to external (subsurface temperature) and internal (ice shelf morphology) perturbations. Defining regions of ice shelves that are critical to ice shelf stability will also narrow the potential range of responses.

3.5. Basal Slope Feedback

[56] Walker *et al.* [2008] analyzed the role of a fixed distribution of basal melting on grounding line retreat,

determining that increased rates near grounding lines were of comparable importance to large changes in the area-averaged melting; basal melting gradients changed the ice shelf profile, grounding line location, and the behavior of the grounded ice upstream.

[57] The results discussed here suggest an instability in the coupled ice-ocean system (the “basal slope feedback”) if the distribution of melting is allowed to vary as a function of ice shelf slope; an intensification of local and cavity-wide melting rates driven by steeper ice shelves may further increase basal melting rates. The initial perturbation may be a change in ocean temperature, but it could also be initiated by a change in grounding line ice flux or the stress regime of the ice shelf.

[58] The coupled response to enhanced entrainment and melting will govern the nature and strength of the basal slope feedback. The change in oceanographic conditions under different ice shelves suggests at least two possibilities. Steeper slopes may increase the heat content of the mixed layer and accelerate the flow, particularly near ice shelf grounding lines. With these ocean-only simulations, increased local melting implies that the ice shelf may assume a more concave shape [Walker and Holland, 2007]. Although the local effect of a steeper slope dominates the response of efficiency in these simulations, it is possible that in a different parameter space, decreases in efficiency could shut off the feedback. Ocean dynamics will be strongly influenced by the glaciological response to changes in melting, reinforcing the need for the development and assessment of a hierarchy of coupled ice-ocean models.

4. Conclusions

[59] In these simulations, large-scale ice shelf thickness gradients foster mixed layer dynamic regimes that control the location and rate of basal melting. Strong, slope-dependent entrainment enhances melting in steep regions; yet inefficiencies are present that limit the use of sub-ice shelf oceanic heat under thinner, less steeply sloped regions of the ice shelf.

[60] In a local heat balance, the mixed layer temperature and melting rate is determined by the ratio of the entrainment rate and the ice-ocean thermal exchange velocity. This ratio also governs the local sensitivity of basal melting to slope and interior ocean temperature. Given the importance of advective heat fluxes and the idealized nature of these simulations, a precise dependence of melting on slope is not presented, yet these results indicate that ice shelf thickness gradients drive comparable along-ice flow gradients in basal melting.

[61] A superlinear dependence of melting is evident under the deepest, fastest-melting part of ice shelves. Ice shelves thus entrain heat and melt disproportionately in steep regions, and they are most sensitive to changes in ice shelf slope in locations that have high basal melting rates. The disproportionate influence of narrow initiation regions near the grounding line underscores the importance of oceanographic constraints on mixing under steeper parts of ice shelves; for models, accurate turbulence parameterizations and an assessment of their sensitivity to spatial resolution are critical.

[62] The use of entrained heat is limited by flow convergence, a key feature of the outflow regime. Because mixed layer flow converges rapidly in these simulations, outflowing seawater has a temperature above the in situ freezing point; it is more sensitive to the interior temperature and the thickness of the mixed layer than the dimensions of the ice shelf. Defining ice-ocean efficiency as the fraction of entrained heat transferred to the ice allows its sensitivity to shape, scale, and temperature to be quantified. Because latent cooling lags increases in entrained heat, ice-ocean efficiency decreases with increasing ocean temperature; the deviation of previous modeling studies from a simple scaling law may result from this advective heat loss.

[63] These simulations indicate that internal dynamics, especially ice shelf shape, exert an influence on basal melting rates that is comparable to that of oceanographic properties outside the ice shelf cavity. Only 20–50% of sub-ice shelf heat is used for melting; small changes in efficiency may modify the response to a change in oceanic forcing. Ice shelf morphology should thus be addressed in climate model parameterizations and in the (presumably more detailed) representation of basal melting incorporated in ice shelf/ice sheet models. The importance of the physics introduced here is scale-dependent; an assessment of each modeling community’s needs, and comparison with observations, are required to extend these findings toward useable parameterizations.

[64] **Acknowledgments.** Doug MacAyeal, Torge Martin, Stan Jacobs, and Rachael Mueller contributed helpful guidance on earlier versions of this manuscript. C.M.L. receives research funding from the United States Environmental Protection Agency (EPA) Science to Achieve Results graduate fellowship program, GFDL (through the Cooperative Institute for Climate Science), and the Science, Technology, and Environmental Policy program in the Woodrow Wilson School of Public and International Affairs at Princeton University. EPA has not officially endorsed this publication, and the views expressed herein may not reflect the views of the EPA.

References

- Beckmann, A., and H. Goosse (2003), A parameterization of ice shelf–ocean interaction for climate models, *Ocean Modell.*, *5*, 157–170, doi:10.1016/S1463-5003(02)00019-7.
- Corr, H. F. J., C. S. M. Doake, A. Jenkins, and D. G. Vaughan (2001), Investigations of an “ice plain” in the mouth of Pine Island Glacier, Antarctica, *J. Glaciol.*, *47*, 51–57, doi:10.3189/172756501781832395.
- Corr, H. F. J., A. Jenkins, K. W. Nicholls, and C. S. M. Doake (2002), Precise measurement of changes in ice-shelf thickness by phase-sensitive radar to determine basal melt rates, *Geophys. Res. Lett.*, *29*(8), 1232, doi:10.1029/2001GL014618.
- Dupont, T. K., and R. B. Alley (2005), Assessment of the importance of ice-shelf buttressing to ice-sheet flow, *Geophys. Res. Lett.*, *32*, L04503, doi:10.1029/2004GL022024.
- Dupont, T. K., and R. B. Alley (2006), Role of small ice shelves in sea-level rise, *Geophys. Res. Lett.*, *33*, L09503, doi:10.1029/2005GL025665.
- Ellison, T. H., and J. S. Turner (1959), Turbulent entrainment in stratified flows, *J. Fluid Mech.*, *6*, 423–448, doi:10.1017/S0022112059000738.
- Gade, H. G. (1979), Melting of ice in sea-water: Primitive model with application to the Antarctic ice shelf and icebergs, *J. Phys. Oceanogr.*, *9*, 189–198, doi:10.1175/1520-0485(1979)009<0189:MOHSW>2.0.CO;2.
- Grosfeld, K., and H. Sandhager (2004), The evolution of a coupled ice shelf–ocean system under different climate states, *Global Planet. Change*, *42*, 107–132, doi:10.1016/j.gloplacha.2003.11.004.
- Hallberg, R. (2000), Time integration of diapycnal diffusion and Richardson number-dependent mixing in isopycnal coordinate ocean models, *Mon. Weather Rev.*, *128*, 1402–1419, doi:10.1175/1520-0493(2000)128<1402:TIODDA>2.0.CO;2.
- Hallberg, R. (2003), The suitability of large-scale ocean models for adapting parameterizations of boundary mixing and a description of a refined bulk mixed layer model, paper presented at Near Boundary Processes and Their Parameterization: 2003 ‘Aha Huliko’a Hawaiian Winter Workshop, Univ. of Hawaii at Manoa, Honolulu, Hawaii.

- Hallberg, R., and A. Gnanadesikan (2006), The role of eddies in determining the structure and response of the wind-driven southern hemisphere overturning: Results from the Modeling Eddies in the Southern Ocean (MESO) project, *J. Phys. Oceanogr.*, *36*, 2232–2252, doi:10.1175/JPO2980.1.
- Hohmann, R., P. Schlosser, S. Jacobs, A. Ludin, and R. Weppernig (2002), Excess helium and neon in the southeast Pacific: Tracers for glacial meltwater, *J. Geophys. Res.*, *107*(C11), 3198, doi:10.1029/2000JC000378.
- Holland, D. M., and A. Jenkins (1999), Modeling thermodynamic ice-ocean interactions at the base of an ice shelf, *J. Phys. Oceanogr.*, *29*, 1787–1800, doi:10.1175/1520-0485(1999)029<1787:MTIOIA>2.0.CO;2.
- Holland, D. M., and A. Jenkins (2001), Adaptation of an isopycnic coordinate ocean model for the study of circulation beneath ice shelves, *Mon. Weather Rev.*, *129*, 1905–1927, doi:10.1175/1520-0493(2001)129<1905:AOAICO>2.0.CO;2.
- Holland, P. R., and D. L. Feltham (2005), Frazil dynamics and precipitation in a water column with depth-dependent supercooling, *J. Fluid Mech.*, *530*, 101–124, doi:10.1017/S002211200400285X.
- Holland, P. R., A. Jenkins, and D. M. Holland (2008), The response of ice shelf basal melting to variations in ocean temperature, *J. Clim.*, *21*, 2558–2572, doi:10.1175/2007JCLI1909.1.
- Jackson, L., R. Hallberg, and S. Legg (2008), A parameterization of shear-driven turbulence for ocean climate models, *J. Phys. Oceanogr.*, *38*, 1033–1053, doi:10.1175/2007JPO3779.1.
- Jacobs, S. S., H. H. Hellmer, and A. Jenkins (1996), Antarctic ice sheet melting in the Southeast Pacific, *Geophys. Res. Lett.*, *23*, 957–960, doi:10.1029/96GL00723.
- Jenkins, A. (1991), A one-dimensional model of ice shelf-ocean interaction, *J. Geophys. Res.*, *96*, 20,671–20,677, doi:10.1029/91JC01842.
- Jenkins, A., and S. Jacobs (2008), Circulation and melting beneath George VI Ice Shelf, *J. Geophys. Res.*, *113*, C04013, doi:10.1029/2007JC004449.
- Joughin, I., and L. Padman (2003), Melting and freezing beneath Filchner-Ronne Ice Shelf, Antarctica, *Geophys. Res. Lett.*, *30*(9), 1477, doi:10.1029/2003GL016941.
- Kader, B. A., and A. M. Yaglom (1972), Heat and mass-transfer laws for fully turbulent wall flows, *Int. J. Heat Mass Transfer*, *15*, 2329–2351, doi:10.1016/0017-9310(72)90131-7.
- Kader, B. A., and A. M. Yaglom (1977), Turbulent heat and mass-transfer from a wall with parallel roughness ridges, *Int. J. Heat Mass Transfer*, *20*, 345–357, doi:10.1016/0017-9310(77)90156-9.
- Lane-Serff, G. F. (1995), On meltwater under ice shelves, *J. Geophys. Res.*, *100*, 6961–6965, doi:10.1029/94JC03244.
- Little, C. M., et al. (2007), Toward a new generation of ice sheet models, *Eos Trans. AGU*, *88*(52), 578, doi:10.1029/2007EO520002.
- Little, C. M., A. Gnanadesikan, and R. Hallberg (2008), Large scale oceanographic constraints on the distribution of melting and freezing under ice shelves, *J. Phys. Oceanogr.*, *38*, 2242–2255, doi:10.1175/2008JPO3928.1.
- MacAyeal, D. R. (1984), Thermohaline circulation below the Ross Ice Shelf: A consequence of tidally induced vertical mixing and basal melting, *J. Geophys. Res.*, *89*, 597–606, doi:10.1029/JC089iC01p00597.
- Makinson, K. (2002), Modeling tidal current profiles and vertical mixing beneath Filchner-Ronne Ice Shelf, Antarctica, *J. Phys. Oceanogr.*, *32*, 202–215, doi:10.1175/1520-0485(2002)032<0202:MTCPAV>2.0.CO;2.
- McPhee, M. G. (1992), Turbulent heat-flux in the upper ocean under sea ice, *J. Geophys. Res.*, *97*, 5365–5379, doi:10.1029/92JC00239.
- McPhee, M. G. (1999), Parameterization of mixing in the ocean boundary layer, *J. Mar. Syst.*, *21*, 55–65, doi:10.1016/S0924-7963(99)00005-6.
- Mellor, G. L., M. G. MCPhee, and M. Steele (1986), Ice-seawater turbulent boundary layer interaction with melting or freezing, *J. Phys. Oceanogr.*, *16*, 1829–1846, doi:10.1175/1520-0485(1986)016<1829:ISTBL>2.0.CO;2.
- Nicholls, K. W., S. Osterhus, K. Makinson, and M. R. Johnson (2001), Oceanographic conditions south of Berkner Island, beneath Filchner-Ronne Ice Shelf, Antarctica, *J. Geophys. Res.*, *106*, 11,481–11,492, doi:10.1029/2000JC000350.
- Nicholls, K. W., et al. (2006), Measurements beneath an Antarctic ice shelf using an autonomous underwater vehicle, *Geophys. Res. Lett.*, *33*, L08612, doi:10.1029/2006GL025998.
- Niiler, P. P., and E. B. Kraus (1977), One-dimensional models of the upper ocean thermocline, in *Modelling and Prediction of the Upper Layers of the Ocean*, edited by E. B. Kraus, pp. 143–172, Pergamon, New York.
- Orsi, A. H., G. C. Johnson, and J. L. Bullister (1999), Circulation, mixing, and production of Antarctic Bottom Water, *Prog. Oceanogr.*, *43*, 55–109, doi:10.1016/S0079-6611(99)00004-X.
- Padman, L., H. A. Fricker, R. Coleman, S. Howard, and L. Erofeeva (2002), A new tide model for the Antarctic ice shelves and seas, *Ann. Glaciol.*, *34*, 247–254.
- Payne, A. J., A. Vieli, A. Shepherd, D. J. Wingham, and E. Rignot (2004), Recent dramatic thinning of largest West Antarctic ice stream triggered by oceans, *Geophys. Res. Lett.*, *31*, L23401, doi:10.1029/2004GL021284.
- Payne, A. J., I. C. Rutt, A. Jenkins, and I. Joughin (2007), Numerical modeling of ocean-ice interactions under Pine Island Bay's ice shelf, *J. Geophys. Res.*, *112*, C10019, doi:10.1029/2006JC003733.
- Pedersen, F. B. (1980), Dense bottom currents in rotating ocean, *J. Hydraul. Div. Am. Soc. Civ. Eng.*, *106*, 1291–1308.
- Pollard, D., and R. M. DeConto (2009), Modelling West Antarctic ice sheet growth and collapse through the past five million years, *Nature*, *458*, 329–333, doi:10.1038/nature07809.
- Price, J. F., and M. O. Baringer (1994), Outflows and deep-water production by marginal seas, *Prog. Oceanogr.*, *33*, 161–200, doi:10.1016/0079-6611(94)90027-2.
- Rignot, E. (2008), Changes in West Antarctic ice stream dynamics observed with ALOS PALSAR data, *Geophys. Res. Lett.*, *35*, L12505, doi:10.1029/2008GL033365.
- Rignot, E., and S. S. Jacobs (2002), Rapid bottom melting widespread near Antarctic ice sheet grounding lines, *Science*, *296*, 2020–2023, doi:10.1126/science.1070942.
- Rignot, E., and K. Steffen (2008), Channelized bottom melting and stability of floating ice shelves, *Geophys. Res. Lett.*, *35*, L02503, doi:10.1029/2007GL031765.
- Schoof, C. (2007), Ice sheet grounding line dynamics: Steady states, stability, and hysteresis, *J. Geophys. Res.*, *112*, F03S28, doi:10.1029/2006JF000664.
- Shepherd, A., D. J. Wingham, and E. Rignot (2004), Warm ocean is eroding West Antarctic Ice Sheet, *Geophys. Res. Lett.*, *31*, L23402, doi:10.1029/2004GL021106.
- Thoma, M., A. Jenkins, D. M. Holland, and S. Jacobs (2008), Modelling Circumpolar Deep Water intrusions on the Amundsen Sea continental shelf, Antarctica, *Geophys. Res. Lett.*, *35*, L18602, doi:10.1029/2008GL034939.
- Walker, R. T., and D. M. Holland (2007), A two-dimensional coupled model for ice shelf–ocean interaction, *Ocean Modell.*, *17*, 123–139, doi:10.1016/j.ocemod.2007.01.001.
- Walker, R. T., T. K. Dupont, B. R. Parizek, and R. B. Alley (2008), Effects of basal-melting distribution on the retreat of ice-shelf grounding lines, *Geophys. Res. Lett.*, *35*, L17503, doi:10.1029/2008GL034947.

A. Gnanadesikan, Geophysical Fluid Dynamics Laboratory, NOAA, Princeton, NJ 08540, USA.

C. M. Little and M. Oppenheimer, Department of Geosciences, Princeton University, Room 28, Guyot Hall, Princeton, NJ 08544, USA. (cmlittle@princeton.edu)